Simulating the circumstellar H_2CO and CH_3OH chemistry of young stellar objects using a spherical physical-chemical model

Fuchs, G.W.; Witsch, D.; Herberth, D.; Kempkes, M.; Stanclik, B.; Chantzos, J.; ... ; Giesen, T.F.

A&A 639, A143 (2020)
https://doi.org/10.1051/0004-6361/202037533

Astronomy & Astrophysics

Simulating the circumstellar H_2CO and CH_3OH chemistry of young stellar objects using a spherical physical-chemical model

G. W. Fuchs[1], D. Witsch[1], D. Herberth[1], M. Kempkes[1], B. Stanclik[1], J. Chantzos[2], H. Linnartz[3], K. M. Menten[4], and T. F. Giesen[1]

[1] Institute of Physics, University Kassel, Heinrich-Plett Str. 40, 34132 Kassel, Germany
e-mail: fuchs@physik.uni-kassel.de
[2] Max-Planck-Institut for Extraterrestrial Physics (MPE), Giessenbachstraße 1, 85748 Garching, Germany
[3] Laboratory for Astrophysics, Leiden Observatory, Leiden University, PO Box 9513, 2300 RA Leiden, The Netherlands
[4] Max-Planck-Institut for Radio Astronomy (MPIfR), Auf dem Hügel 69, 53121 Bonn, Germany

Received 20 January 2020 / Accepted 20 April 2020

ABSTRACT

Context. Young stellar objects (YSOs) and their environments are generally geometrically and dynamically challenging to model, and the corresponding chemistry is often dominated by regions in non-thermal equilibrium. In addition, modern astrochemical models have to consider not only gas-phase reactions, but also solid-state reactions on icy dust grains. Solving the geometrical, physical, and chemical boundary conditions simultaneously requires a high computational effort and still runs the risk of false predictions due to the intrinsically non-linear effects that can occur. As a first step, solving problems of reduced complexity is helpful to guide more sophisticated approaches.

Aims. The objective of this work is to test a model that uses shell-like structures (i.e., assuming a power-law number density and temperature gradient of the environment surrounding the YSO) to approximate the geometry and physical structure of YSOs, that in turn utilizes an advanced chemical model that includes gas-phase and solid-state reactions to model the chemical abundances of key species. A special focus is set on formaldehyde (H_2CO) and methanol (CH_3OH) as these molecules can be traced in the gas phase but are produced on icy dust grains. Furthermore, this kind of molecule is believed to be key to understanding the abundance of more complex species. We compare the influence of the geometry of the object on the molecular abundances with the effect induced by its chemistry.

Methods. We set up a model that combines a grain-gas phase chemical model with a physical model of YSOs. The model ignores jets, shocks, and external radiation fields and concentrates on the physical conditions of spherically symmetric YSOs with a density and temperature gradient derived from available spectral energy distribution observations in the infrared. In addition, new observational data are presented using the APEX 12 m and the IRAM 30 m telescopes. Formaldehyde and methanol transitions have been searched for in three YSOs (R CrA-IRS 5A, C1333-IRAS 2A, and L1551-IRS 5) that can be categorized as Class 0 and Class 1 objects, and in the pre-stellar core L1544. The observed abundances of H_2CO and CH_3OH are compared with those calculated by the spherical physical-chemical model.

Results. Compared to a standard "ρ and T constant" model, i.e., a homogeneous (flat) density and temperature distribution, using number density and temperature gradients results in reduced abundances for the CO hydrogenation products formaldehyde and methanol. However, this geometric effect is generally not large, and depends on the source and on the molecular species under investigation. Although the current model uses simplified geometric assumptions the observed abundances of H_2CO and CH_3OH are well reproduced for the quiescent Class 1 object R CrA-IRS 5A. Our model tends to overestimate formaldehyde and methanol abundances for sources in early evolutionary stages, like the pre-stellar core L1544 or NGC 1333-IRS 2A (Class 0). Observational results on hydrogen peroxide and water that have also been predicted by our model are discussed elsewhere.

Key words. astrochemistry – molecular processes – stars: protostars – ISM: molecules

1. Introduction

It is interesting to reflect on the origin of the chemical content of our solar environment that allowed the creation of life-supporting molecular species, and it is widely believed that the study of the chemistry of young stellar objects (YSOs) will bring us closer to a basic understanding of this topic. Today these YSOs can be studied in great detail using images from the *Hubble* space telescope (Padgett et al. 1999) or other observatories (Lucas et al. 1997; Close et al. 1997). The images show that these objects can be full of substructures on various scales, resulting in dynamically complex patterns. Depending on the age and history of such an object it can be thought of as consisting of an extended envelope, an accretion disk with a protostar located at its center, cavities, a jet and possibly shock regions, and pronounced interaction zones with central and external radiation fields. Here, in different regions different chemical processes may take place. Molecules are often used as chemical probes for these regions, which can also provide information about the local physical conditions like density and temperature (Bruderer et al. 2009a). In this work we are particularly interested in a chemical network that enables the emergence of complex organic molecules (COMs) and the associated formation of water. It is believed that chemical reactions on grain surfaces and in cryogenic solids (ices) play an important role in the formation of precursor molecules of water and of COMs, like H_2CO or

CH_3OH (Garrod et al. 2008; Du et al. 2012; Lee et al. 2019). A truly faithful model that takes into account multi-dimensional geometric aspects and a chemistry that in some regions is far from a thermal equilibrium is computationally very demanding and, due to the complexity of this task and to non-linear effects that can occur, not necessarily of superior predictive power. The challenges are therefore twofold. On the one hand, an underlying geometry must be realistic enough but not too complex to be comprehensible; on the other hand, complex chemical processes must be modeled sufficiently correctly, i.e., also including gas-grain interactions. Early models of star forming regions assumed a fixed density and temperature (Leung et al. 1984), but quickly models were developed that also considered space-dependent chemistry (e.g., Caselli et al. 1993; Millar et al. 1997) or were adapted to observations under the assumption of spherical symmetry with 1D physical parameters (Doty et al. 2002; Stäuber et al. 2005). Bruderer et al. (2009a,b) introduced a 2D axisymmetric chemical model of YSO envelopes. The model we present here is not of the latter kind. It works with a simplified geometric model that we consider sufficient for our purpose, i.e., it concentrates on the envelope of YSOs, regions that can be considered equivalent to our outer solar system region extending to the Oort cloud where premordial comets originate. Our model assumes spherically symmetric YSOs with a density and temperature gradient based upon spectral energy distributions (SEDs) derived from infrared observations (Robitaille et al. 2007; Kristensen et al. 2012). There have been other in-depth studies and tests of models of YSOs, some of which also used power-law density models (Hogerheijde et al. 2010). Other studies focused more on the dynamical aspects or photon-induced chemistry (Stäuber et al. 2005; Bruderer et al. 2009a). Our chemical model is based on the work of Du et al. (2012) and includes gas-phase and solid-state reactions.

Compared to the gas-phase only a few molecules have been identified as solid components in cosmic ices, with H_2O, CO, CH_3OH, H_2CO, HCOOH, CO_2, NH_3, and NH_4^+ being typical examples (Tielens & Hagen 1982; Whittet et al. 1996; Boogert et al. 2015). Thus, not only is water ice (and presumably the precursor hydrogen peroxide) formed on cold grains, formaldehyde (H_2CO) and methanol (CH_3OH) ices have also been observed (Boogert et al. 2008; Bottinelli et al. 2010). In the laboratory the underlying hydrogenation reaction chain has been investigated on carbon monoxide (CO) interstellar ice analogs (Fuchs et al. 2009; Hiraoka et al. 2002; Watanabe & Kouchi 2002). Starting with solid CO, atomic hydrogen (H) addition leads to the intermediate HCO and subsequently to H_2CO. With ongoing hydrogenation, formaldehyde can further react to the intermediate H_3CO resulting in CH_3OH fractions in the ice. Depending on the initial ice content (e.g., the amount of solid CO and O_2), the production of HOOH and H_2O, and of H_2CO and CH_3OH, can proceed simultaneously. In some recent work abstraction reactions along this chain were shown to provide additional pathways in the formation of H_2CO in CO ices, and to molecules larger than methanol, like glycol aldehyde, ethylene glycol, and glycerol (Chuang et al. 2016; Fedoseev et al. 2017). Carbon monoxide and molecular oxygen accrete on the grains at about the same temperature, but the abundance of CO is much higher. In the laboratory the hydrogenation of mixed CO and O_2 ices results in H_2CO and CH_3OH, as well as HOOH and H_2O, but also in the formation of CO_2 via the reactive intermediate HOCO, which links the CO and O_2 hydrogenation chains (see Fig. 2 in Ioppolo et al. 2011). The reaction efficiencies of CO+H and O_2+H seem to be comparable, but depend on the initial CO/O_2 ratio. For this reason we also include HOOH and H_2O in this work as their formation scheme is connected to that of H_2CO and CH_3OH. However, in contrast to formaldehyde and methanol, HOOH has not been identified in interstellar ices via infrared absorption observations, but only as a gas-phase species via (sub)millimeter emission observations (Bergman et al. 2011; Smith et al. 2011; Fuchs et al. 2020). Du et al. (2012) included a desorption mechanism in their model based on the release of excess energy during the solid-state molecule formation, as did Chuang et al. (2018) for reactive desorption processes of CO hydrogenation products (see also Cazaux et al. 2016; Minissale et al. 2016). Our aim is to estimate molecular abundances of key molecules like H_2CO and CH_3OH in the gas phase (which are assumed to have formed in the solid phase during the early phases of YSOs) by combining the results of the chemical model from Du et al. (2012) with the assumption of a spherical gradient distribution of the density and temperature. Using our combined physical-chemical model (see Sect. 2) we present in Sect. 5 predictions of H_2CO and CH_3OH abundances in the close-by YSOs L1551-IRS 5, R CrA-IRS 5A, and NGC 1333-IRAS 2A, and in the pre-stellar core L1544 (Sects. 3 and 4) and compare them with astronomically derived values (Sect. 6).

2. Physical-chemical shell model

2.1. Physical parameters

In our approach the results of the chemical calculations done by Du et al. (2012) are used in a physical model of astronomical sources that show spherical symmetry with a power-law number density and temperature gradient $\rho_N(r) \sim r^{-p}$ and $T(r) \sim r^{-b}$, with p and b being specific source parameters as listed in Table 1 and $r \geq r_{\rm start} > 0$ given in [AU] [1]. Here $r_{\rm start}$ defines the distance to the star from which substantial contributions to molecule formation are expected. This will be discussed later in more detail. In the model the highest densities and temperatures can be found close to the central protostar, which then decrease as a function of the distance r to the central object (except for the source L1544 where the temperature is nearly constant or lowest at the center, and the model had to be adjusted accordingly). The values for the physical model were mainly taken from Kristensen et al. (2012) and are based on dust emission observations and subsequent analysis of the SED using the DUSTY code (Ivezic & Elitzur 1997; see also similar earlier work by Schöier et al. 2002). DUSTY is a 1D spherically symmetric dust radiative transfer code. For our model we used the source parameters p and q and the innermost radius $r_{\rm in}$ (which is defined as the radius where $T = 250$ K) to calculate the density and temperature at a given radius within the YSO envelope. Here q is a source-specific proportionality factor ($\rho_N = q \cdot r^{-p}$), as given in Table 1. No structures other than the envelope (i.e., jet outflows or non-symmetrical contributions) are considered (see Fig. 1). More specifically, for CrA-IRS 5A the values given in Lindberg & Jørgensen (2012) have also been used to calculate the temperature gradient; for the pre-stellar core L1544 the parameters were taken from Caselli et al. (2002).

[1] The term, and the values, of $r_{\rm in}$ and $r_{\rm out}$ in Table 1 are taken from the references given in the table and are used to determine the constants q, p, a, and b. The term $r_{\rm start}$, and also the later introduced term $r_{\rm end}$, is specific to our model and is not the same as $r_{\rm in}$ and $r_{\rm out}$. The definition of $r_{\rm start}$ and $r_{\rm end}$ is explained later in the text. In brief, $r_{\rm start}$ and $r_{\rm end}$ set the integration limits of our model, i.e., they define the region that is considered.

Table 1. Physical parameters of observed objects.

Source	ρ_{source} [cm^{-3}]		T_{source} [K]		r_{in} [AU]	r_{out} [10^4 AU]	age τ [yr]	References
	q	p	a	b	(250 K)	(10 K)		
R CrA-IRS 5A	7×10^7	0.8	735.5	0.467	10	1.0	6×10^5 (1)	[1,2]
NGC 1333-IRAS 2A	2×10^{11}	1.7	473.4	0.392	36	1.7	$\sim2\times10^4$ (2)	[1]
L1551-IRS 5	3×10^{11}	1.8	1440.4	0.521	29	~1.4	6×10^5 (1)	[1]
L1544	1.26×10^6	0.0	12.5 (3)	0.000			5×10^4 (4)	[3,4]

Notes. The number density is calculated using $\rho_N = q \cdot r^{-p}$ in [cm^{-3}] with r given in [AU]. The temperature is given by $T = a \cdot r^{-b}$ in [K] with r given in [AU]. The parameter p is taken from the given literature (reference), whereas q, a, and b are calculated from boundary conditions like n_{in} and n(1000 AU), or r_{in} and r(10 K) in the given reference. (1)Average Class I object age. (2)Chemical age of source taken from Brinch et al. (2009); Jørgensen et al. (2004a). (3)The temperature is fixed, i.e., no temperature gradient is assumed (pre-stellar core). (4)Chemical age of source taken from Bizzocchi et al. (2014).

References: [1] Kristensen et al. (2012); [2] Lindberg & Jørgensen (2012); [3] Caselli et al. (2002); [4] Bizzocchi et al. (2014).

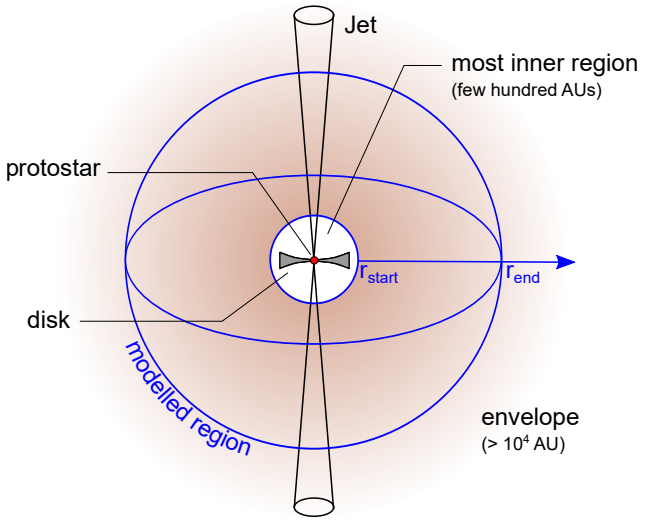

Fig. 1. Sketch of the applied physical model geometry for protostellar objects. The integrated region (blue-edged hollow sphere) excluding the innermost and outermost parts is the region used for the calculations. The envelope of the object exceeds r_{end} and has a diameter larger than 10^4 AU. The jet and disk have not been taken into account in our model.

2.2. Chemical model

The chemical model used is completely based on the work by Du et al. (2012) and has been described there in detail (see also Du & Parise 2011). In brief, the gas phase chemistry is based on the UMIST RATE06 network[2] (Woodall et al. 2007). In total 284 gas phase species connected via 3075 gas phase reactions were included, but species containing Fe, Na, Mg, and Cl were excluded. The initial conditions are the same as in Stantcheva & Herbst (2004)[3]. To model the gas-grain chemistry the hybrid moment equation (HME) approach was used (see Du & Parise 2011). The cosmic-ray ionization rate used is 1.36×10^{-17} s^{-1} (canonical value; see Woodall et al. 2007). In total, 151 surface reactions and 56 surface species were taken into account (Allen & Robinson 1977; Tielens & Hagen 1982; Hasegawa et al. 1992), with binding energies of surface species based on Hasegawa & Herbst (1993) and Garrod (2008b). In particular, the ice-borne molecules H_2CO, CH_3OH, HOOH, and H_2O are included and their corresponding surface reaction routes are briefly outlined below.

The hydrogenation of CO results in the formation of H_2CO and CH_3OH via

$$CO \xrightarrow{H} HCO \xrightarrow{H} H_2CO \xrightarrow{H} H_3CO \xrightarrow{H} CH_3OH$$

and is based on laboratory work by Fuchs et al. (2009), Hiraoka et al. (2002), and Watanabe & Kouchi (2002). We also included the solid-state formation of water on grain surfaces in the model (Cuppen et al. 2010).

There are critical parameters, namely the source age, density, and temperature, that largely determine the accuracy of our predictions. Unfortunately, in the case of the very critical age dependence exact numbers are often not at hand and only the general stage classification (Class 0 or 1) is available. Therefore, we estimated the effect of the source age on the abundance and temperature uncertainty by varying the source age as input parameter.

Using the input parameters in Table 1, our model predicts the abundance ratio $A = [X]/[\text{hydrogen}]$ and number density ρ_X of each molecule X of interest at a given radius to the central star. An example is shown in Fig. 2, where the used model values are shown for the hydrogen density and temperature (top graph) along the distance axis for the source R CrA-IRS 5A. The model output data is shown in the graph below, with the number densities of H_2CO, CH_3OH, H_2O and HOOH. As can be seen, these molecules are only formed in a shell-like region around the star with a void region at the center and a fall-off at larger radii. The innermost region (i.e., the first few hundred AUs where a disk structure may or may not exist depending on the age of the source) is not considered; instead, we focus on the surrounding still in-falling material of the YSO (see Table 2).

The total number of molecules is calculated by integrating ρ_X over the source volume and subsequently the column density N_c is determined[4]. The integration starts at a distance r_{start} from the star at which significant molecule production occurs; see Fig. 1. The reason for this limitation (r_{start}) is that, especially for more evolved sources like Class 1 YSOs, at the very center of these objects the geometry is not centro-symmetric but disk-like. Thus, our gradient density law (and temperature law) fails in the inner

[2] http://udfa.net

[3] See Stantcheva & Herbst (2004) Table 1 for initial fractional abundances.

[4] Opposed to the column density, the total number of particles is an intrinsic source parameter independent of the line of sight. This number is useful when comparing different models, such as homogeneous and non-homogeneous density and temperature distribution models; see Sect. 2.3.

Table 2. Parameters used in the shell model and resulting mean temperature and density of hydrogen.

Source	Integration settings [a]	Integration limits (radii) r_{start}/T_{up} [AU]/[K]	r_{end}/T_{low} [AU]/[K]	Emission [b] region (model) [″]	$\bar{T}(H_2)$ [c] [K]	$\bar{N}_c(H_2)$ [d] [cm^{-3}]	H_2 particle number [e] [#]
R CrA-IRS 5A	A	72/100	10 000/10	153.″8	12.7	6.1×10^4	8.5×10^{56}
	B	683/35	4 194/15	64.″5	18.6	1.2×10^5	1.2×10^{56}
NGC 1333-IRAS 2A	A	207/100	17 000/10	144.″7	16.2	3.2×10^4	2.2×10^{57}
	B	1546/35	7823/15	66.″6	20.5	1.1×10^5	7.0×10^{56}
L1551-IRS 5	A	168/100	14 000/10	200.″0	16.9	2.6×10^4	9.9×10^{56}
	B	1265/35	6425/15	91.″8	20.7	9.1×10^4	3.4×10^{56}
L1544	C	1/12.5	8000/12.5	114.″3	12.5	1.3×10^6 [f]	9.1×10^{57}

Notes. [a]Two integration settings have been used (A, B) starting at r_{start} and ending at r_{end} depending on the temperature region to be covered (A = 10–100 K, and B = 15–35 K), C indicates a flat density and temperature distribution of hydrogen. [b]Outer diameter of region where our investigated molecules, e.g., H_2CO or CH_3OH, emit radiation according to our model. [c]Hydrogen mean temperature. [d]Hydrogen mean particle density. [e]Absolute number of hydrogen particles within integration limits. This number is used to calculate the $\overline{[X]/[H_2]}$ values in Tables 3 and 4. [f]Value from Caselli et al. (2002) for inner 40″ region.

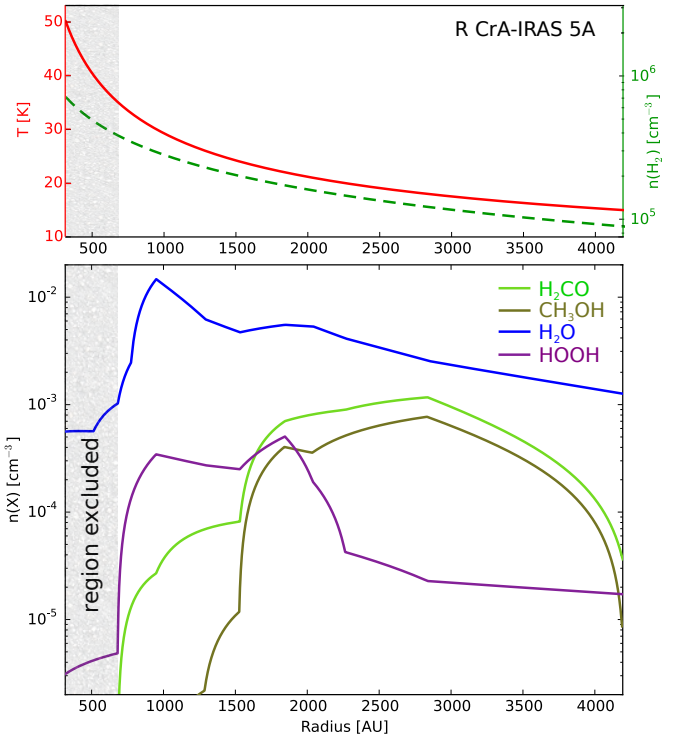

Fig. 2. Shell model of R CrA-IRS 5A. *Top*: temperature (solid red) and hydrogen density (dashed green) are given as a function of the distance to the central star. *Bottom*: number density n of the molecules H_2CO, CH_3OH, H_2O and HOOH is shown (light green, dark green, blue and purple, respectively). The region at low radii (gray area at left) has been excluded from the abundance calculations of the species.

region and would overestimate the number densities. The chosen starting distance is source and molecule (X) dependent and can, in addition to the hydrogen density, mainly be chosen by suitable temperature T_{start} conditions at the distance r_{start} from the center. Obviously, there is no clear cut-off condition for the integration limits, and numbers have been chosen based on reasonable estimates, as outlined below. In addition, the calculations over large volumes proved to be very time consuming, and thus we worked with two different data sets. Table 2 lists the used integration limits, with set A resulting in a wide shell-like region around the star that also includes the very inner region (here the inner region reaches 100 K and the outer 10 K); set B is a much smaller subregion of A in which the targeted molecules are produced most abundantly (with temperatures between 35 and 15 K). The model values of set B can be achieved in much less time than those of set A, but they are still very close to those of set A. For example, as can be seen from the absolute particle numbers $N(X)_{total}$, $92 \pm 3.6\%$ of H_2CO and $98 \pm 0.5\%$ of CH_3OH is already contained in region B. Thus, in most cases it is sufficient to do the analysis for region B alone. The reason why region B already includes the most particles of our investigated species is as follows. When looking at the conditions for HOOH (rather than for H_2CO or CH_3OH) we see that at temperatures above 30 K the HOOH production is strongly reduced as O_2 cannot freeze out on the grain surfaces, and thus no efficient surface-based hydrogenation can take place. Since at 35 K the HOOH production nearly ceases completely, we chose the corresponding inner radius (r_{start}) as the starting point for the integration (i.e., for case B). For H_2CO and CH_3OH the appropriate cut-off temperature is even lower, and accordingly a larger $r_{start}(X)$ value than r_{start}(HOOH) could in principle be used. However, for the sake of comparability, we use the smaller value r_{start}(HOOH) for all species for a given source in set B. In that way the integration range always includes the regions that are essential for all discussed species. In the calculations the region around the central object has been divided into shells with each region having a certain hydrogen density and temperature. Our model does not allow the mixing of particles between these shells. The chemistry of the shells is determined individually, and by assuming a steady transition between these zones the overall content of molecules is calculated. In Fig. 2 the case of R CrA-IRS 5A is displayed. We use $r_{start} \approx 680$ AU for all investigated species, with the local temperature being 35 K. The upper integration limit is $r_{end} \approx$ 4200 AU corresponding to 15 K temperature where the mobility of particles on the grain surfaces is already strongly reduced.

Finally, the column density $N_c(X)$ is calculated by putting the total number of species X within the given integration range (corresponding to a certain volume) in proportion to the cross section of the calculated sphere. We calculated two types of column

Table 3. Shell model results for H_2CO and CH_3OH.

Molecule/ source	Inte- gration settings [(a)]	Gradient model (shell-like structure)						
		$\bar{T}(X)$ [K]	$\bar{\rho}(X)$ [cm^{-3}]	ρ_{max}(X) at distance [cm^{-3}] at [AU]	$N(X)_{total}$ [#]	$\overline{[X]/[H_2]}$	N_c^1(X) ($r_{start} - r_{end}$) [cm^{-2}]	N_c^2(X) ($\theta_{mb} = 25''$) [cm^{-2}]
H_2CO								
R CrA-IRS 5A	A	17.4	4.4×10^{-5}	1.1×10^{-3} at 2837	6.2×10^{47}	7.3×10^{-10}	8.8×10^{12}	6.3×10^{13}
	B	18.1	5.3×10^{-4}	1.1×10^{-3} at 2837	5.4×10^{47}	4.4×10^{-10}	4.4×10^{13}	6.1×10^{13}
NGC 1333-IRAS 2A	A	18.2	1.2×10^{-4}	2.4×10^{-3} at 5519	8.2×10^{48}	3.8×10^{-9}	4.0×10^{13}	2.5×10^{14}
	B	18.5	1.2×10^{-3}	2.4×10^{-3} at 5519	7.7×10^{48}	1.1×10^{-8}	1.8×10^{14}	2.4×10^{14}
L1551-IRS 5	A	18.2	3.6×10^{-5}	7.5×10^{-4} at 4408	1.4×10^{48}	1.4×10^{-9}	1.0×10^{13}	6.0×10^{13}
	B	18.5	3.6×10^{-4}	7.5×10^{-4} at 4408	1.3×10^{48}	3.9×10^{-9}	4.5×10^{13}	5.9×10^{13}
L1544	C	12.5	2.9×10^{-4}		2.1×10^{48}	2.3×10^{-10}	4.6×10^{13}	6.8×10^{13}
CH_3OH								
R CrA-IRS 5A	A	17.8	2.5×10^{-5}	7.6×10^{-4} at 2838	3.6×10^{47}	4.2×10^{-10}	5.1×10^{12}	3.7×10^{13}
	B	17.9	3.4×10^{-4}	7.6×10^{-4} at 2838	3.5×10^{47}	2.8×10^{-9}	2.8×10^{13}	3.7×10^{13}
NGC 1333-IRAS 2A	A	18.1	3.2×10^{-4}	7.2×10^{-3} at 5519	2.2×10^{49}	1.0×10^{-8}	1.1×10^{14}	6.1×10^{14}
	B	18.1	3.2×10^{-3}	7.2×10^{-3} at 5519	2.1×10^{49}	3.0×10^{-8}	5.0×10^{14}	6.0×10^{14}
L1551-IRS 5	A	18.1	2.6×10^{-5}	6.0×10^{-4} at 4526	1.0×10^{48}	1.0×10^{-9}	7.3×10^{12}	4.0×10^{13}
	B	18.2	2.7×10^{-4}	6.0×10^{-4} at 4526	9.9×10^{47}	2.9×10^{-9}	3.4×10^{13}	3.9×10^{13}
L1544	C	12.5	1.2×10^{-4}		8.8×10^{47}	9.8×10^{-11}	2.0×10^{13}	2.9×10^{13}

Notes. Comment: $\bar{T}(X)$ is the mean temperature in the shell between $r_{start} - r_{end}$ and $\bar{\rho}(X)$ is the mean particle density in that region. The sum of all molecules ($X = H_2CO$ or CH_3OH) is denoted as $N(X)_{total}$ and $\overline{[X]/[H_2]}$ is the mean ratio of the species [X] and hydrogen in the region. The column density $N_c(X)$ is calculated (1) for the region between $r_{start} - r_{end}$, i.e., $N(X)_{total}$ divided by πr_{end}^2, and (2) as column density along the line of sight of the telescope main beam $\theta_{mb} = 25''$, i.e., at typical main beam diameters of APEX 12 m (242 GHz) and IRAM 30 m (97 GHz); see Fig. 3. The definition of the integration settings A, B, and C is given in Table 2. [(a)]For integration setting details see Table 2.

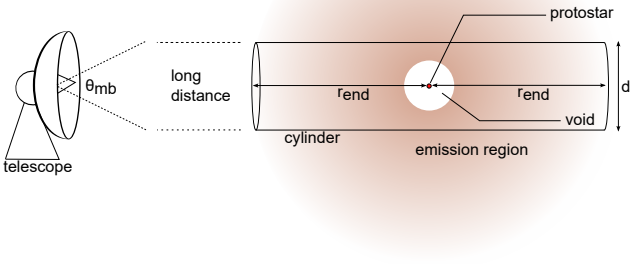

Fig. 3. Cylindrical region used to calculate the column density $N_c^2(X)$ as subset of the emission region around the star. The top hat diameter (d) corresponds to the telescope main beam lobe opening angle θ_{mb}. Only particles in the volume $0.5\,\pi\,r_{end}\,d^2$ are considered.

densities, which are indicated by superscripts 1 and 2[5]: $N_c^1(X)$ is calculated using all molecules within the radii r_{start} and r_{end} (i.e., $N(X)_{total}$ divided by πr_{end}^2) and is the overall average column density; $N_c^2(X)$ is the column density along the line of sight of the telescope with a main beam lobe of $\theta_{mb} = 25''$ (i.e., at typical main beam diameters of APEX 12 m at 242 GHz, and IRAM 30 m at 97 GHz; see Fig. 3). In Table 3 the results of the calculation are listed assuming that the age of the source is accurately determined. No uncertainties are given. The differences in the given column densities between sets A and B result in the much larger cross section of set A compared to set B, whereas the absolute particle number in both cases is nearly identical. A more useful number for observations with radio telescopes is the column density $N_c^2(X)$, which corresponds to the main beam lobe of the telescope (θ_{mb}) and is calculated by the integration of the number density within the cylindrical volume defined by θ_{mb} ($\hat{=}$ diameter d) that stretches along the line of sight as shown in Fig. 3. As θ_{mb} is a function of the wavelength we only give a representative value for $\theta_{mb} = 25''$ in Table 3. It can be seen that the differences between $N_c^2(X)$ of the set A and B are negligible and that $N_c^2(X)$ is close to the value $N_c^1(X)$ for set B, as is expected.

[5] To avoid confusion with the total number of species N, the column density N_c has the subscript "c".

2.3. First tests

Our model reproduces the values by Du et al. (2012) for the known source ρ Oph A with constant ρ and T nearly exactly, and is thus consistent with the previous study of this source.

Comparison with "flat" model. In a second step, we investigated what effect the gradients of the H_2 density and temperature (i.e., our geometrical assumptions) have on the molecule abundances. To do this, we compared the results of our "gradient" model given in Table 3 with the abundance values that were calculated using a constant density and temperature over the assumed source size. In the flat model we used the hydrogen mean temperature, number density, and absolute particle

Table 4. Results for H_2CO and CH_3OH from the flat model based on constant densities and constant temperatures.

Molecule/ source	Inte- gration settings [(a)]	Flat model (homogeneous structure) $\bar{T}(X)$ [K]	$\bar{\rho}(X)$ [cm^{-3}]	$N(X)_{total}$ [#]	$\overline{[X]/[H_2]}$	$N_c^1(X)$ ($r_{start} - r_{end}$) [cm^{-2}]	$N_c^2(X)$ ($\theta_{mb} = 25''$) [cm^{-2}]	Comparison of models $N(X)_{total}$(flat) / $N(X)_{total}$(gradient)
H_2CO								
R CrA-IRS 5A	B	18.6	1.0×10^{-3}	1.0×10^{48}	8.5×10^{-9}	8.5×10^{13}	1.2×10^{14}	1.92
NGC 1333-IRAS 2A	B	20.5	1.6×10^{-3}	1.1×10^{49}	1.5×10^{-8}	2.5×10^{14}	3.5×10^{14}	1.39
L1551-IRS 5	B	20.7	4.87×10^{-4}	1.8×10^{48}	5.3×10^{-9}	6.2×10^{13}	8.5×10^{13}	1.36
CH_3OH								
R CrA-IRS 5A	B	18.6	6.7×10^{-4}	6.9×10^{47}	5.6×10^{-9}	5.6×10^{13}	8.0×10^{13}	2.00
NGC 1333-IRAS 2A	B	20.5	3.9×10^{-3}	2.6×10^{49}	3.7×10^{-8}	6.0×10^{14}	8.5×10^{14}	1.22
L1551-IRS 5	B	20.7	3.1×10^{-4}	1.1×10^{48}	3.3×10^{-9}	3.9×10^{13}	5.4×10^{13}	1.14

Notes. [(a)]For integration setting details see Table 2. Here r_{end} is used as integration radius.

numbers given in Table 2. This means that in both calculations the chemical network is the same, only the physical parameters ρ and T are different. Thus, instead of having a hydrogen density gradient in our chemical calculations a constant density $\bar{\rho}$ was used for all radii and a constant average temperature $\bar{T}$. Naturally, this resulted in a different outcome of the investigated molecular species (see Table 4). In all cases, except L1544 where the gradient model is not used anyway, the molecule abundances of H_2CO and CH_3OH in a gradient model were lower by 14–100% depending on the examined molecule and source compared to the flat model. In the case of HOOH and H_2O (not shown in the table) we saw differences of up to 800%, i.e., the hydrogen peroxide and water abundance can be strongly overestimated in the flat model compared to a gradient model. This means that using the gradient model generally results in more conservative abundances, and consequently reduces the amount of objects that seem suitable for observations when compared with the standard ρ and T constant model. Nevertheless, it seems worthwhile mentioning that even in the worst case this geometric effect is not large (not even an order of magnitude) and cannot account for large discrepancies between modeled and observed abundances.

The age uncertainty problem. Our model is sensitive to the age of the investigated object. In each of the sublayers (shells) the chemistry evolves separately in time according to the age of the object. The geometry does not change during this time evolution, and is only given by the geometric parameters fixed in Table 1. This scenario greatly simplifies the problem and most likely does not correspond to reality; however, due to the strongly increased complexity a simultaneous co-evolution of physical and chemical parameters was not realized in our model. Unfortunately, the age of the sources is very often not known to high precision, which results in a large uncertainty of the calculated values. To estimate the resulting uncertainties we varied the ages of the sources as given in Table 1 by ±30% (see Table 5). In our model, the changes in the absolute particle numbers $N(X)_{total}$ and column densities $N_c^1(X)$ and $N_c^2(X)$ are different when assuming 30% less or 30% more time for the object, an asymmetry that also exists for a flat model and which reflects the complicated chemical evolution with time (see Fig. 1 in Du et al. 2012). The resulting uncertainties are large, i.e., on the order of the mean value itself.

Table 5. Results of robustness test for object age using an age variation ±30% to estimate column density uncertainties for H_2CO and CH_3OH.

Molecule/ source	$N(X)_{total}$ [10^{47} #]	$N_c^1(X)$ ($r_{start} - r_{end}$) [10^{13} cm^{-2}]	$N_c^2(X)$ ($\theta_{mb} = 25''$) [10^{13} cm^{-2}]
H_2CO			
R CrA-IRS 5A	$5.4^{+4.7}_{-1.7}$	$4.4^{+3.7}_{-1.4}$	$6.1^{+5.2}_{-2.0}$
NGC 1333-IRAS 2A	77^{+39}_{-7}	18^{+9}_{-2}	$24^{+12.7}_{-1.9}$
L1551-IRS 5	13^{+12}_{-4}	$4.5^{+4.0}_{-1.4}$	$5.9^{+5.0}_{-1.9}$
L1544	21^{+9}_{-6}	$4.6^{+2.1}_{-1.3}$	$6.8^{+3.3}_{-1.9}$
CH_3OH			
R CrA-IRS 5A	$3.5^{+3.4}_{-0.8}$	$2.8^{+2.7}_{-0.6}$	$3.7^{+3.5}_{-0.8}$
NGC 1333-IRAS 2A	210^{+31}_{-5}	$50^{+6.1}_{-2.4}$	$60^{+8.3}_{-2.0}$
L1551-IRS 5	$9.9^{+9.7}_{-2.0}$	$3.4^{3.4}_{-0.7}$	$3.9^{+3.9}_{-0.8}$
L1544	$8.8_{(-6.7)}$	$2.0_{(-1.5)}$	$2.9_{(-2.2)}$

Notes. Setting B has been used; see Table 2 for details. The calculations are based on a gradient density and temperature distribution; see Table 3. The given uncertainties are based on the assumption that the true age can vary by ±30% of the given age listed in Table 1.

Recommended values. For convenience and to ease comparison, the recommended model values for N_c and T are summarized in Table 8 along with the results of our observations which are discussed in Sect. 5. As can be seen, the recommended values are close to those of set B and C in Table 3. The uncertainty values are estimated from variations in the source age and boundary conditions (i.e., using the more conservative values of set B, and temperature changes of ±1 K (i.e., ∼10% of absolute value).

3. Astronomical sources

Based on an extensive list of pre- and protostellar objects (e.g., Kristensen et al. 2012; Mottram et al. 2014), we selected those sources that are the most promising candidates to test our new physical-chemical model and that are within reach of either the APEX 12 m or the IRAM 30 m telescope, namely R CrA-IRS 5A, NGC 1333-IRAS 2A, L1551-IRS 5, and L1544. The

selected sources have in common that water has been detected towards these objects and that the predicted amount of HOOH in these sources is enough to be detected. Observational details of all four investigated sources are given in Fuchs et al. (2020). Here we briefly summarize the H_2CO and CH_3OH observations of these sources that have been published prior to this work.

L1544 (pre-stellar core). This object is a starless low-mass star forming region in the constellation Taurus (Crapsi et al. 2005, 2007). There have been previous investigations of formaldehyde (H_2CO) by Tafalla et al. (1998) and Young et al. (2004) and methanol (CH_3OH; Jiménez-Serra et al. 2016; Punanova et al. 2018). Both molecules have been detected in this source. L1544 can be modeled with a simple flat temperature and density distribution according to Caselli et al. (2002).

NGC 1333-IRS 2A (Class 0). NGC 1333-IRS 2A is a typical Class 0 object (Brinch et al. 2009) located in the constellation Perseus. It is a binary system with an associated molecular jet and bow shock (Sandell et al. 1994). Observations of H_2CO and CH_3OH have been performed by Maret et al. (2004, 2005), Jørgensen et al. (2005), and Bottinelli et al. (2007). Due to the complex structure we decided to investigate three separate spatial regions of this source: IRS 2A-1 (center position), IRS 2A-2 (off-center), and IRS 2A-1 (in center line to north–south outflow).

R CrA-IRS 5A (Class 1). The source IRS 5 (Taylor & Storey 1984) is located in Corona Australis close to the star R CrA. Formaldehyde and methanol have been detected in this source by Lindberg et al. (2015).

L1551-IRS 5 (Class 1). The close-by young stellar object L1551 is a Class 1 source with a core binary system in the Taurus molecular cloud complex (Osorio et al. 2003; Lee et al. 2014; Ainsworth et al. 2016). This object is associated with molecular outflows and shock regions (Snell et al. 1980). H_2CO (Sandqvist & Bernes 1980; Duncan et al. 1987) and CH_3OH (White et al. 2006) have been detected in this source.

4. Observations and data reduction

The observations were performed using the APEX 12 m and IRAM 30 m telescopes (see Fuchs et al. 2020 for observational and data analysis details). In brief, in September 2015 we used the APEX 12 m telescope at three selected wavelengths between 0.9 mm and 1.3 mm for observations on R CrA-IRS 5A and NGC 1333-IRAS 2A[6]. The observations using the IRAM 30 m telescope at the Pico del Veleta in Spain towards L1551-IRS 5 and L1544 were done in August 2016[7] at four selected wavelengths between 1.3 and 3.3 mm. L1551 has been investigated in position switching mode as well as in frequency switching mode, whereas L1544 has been observed in frequency switching mode only. The basic data reduction and processing was done using the Continuum and Line Analysis Single-dish Software (CLASS) from the GILDAS[8] software package. The observations were analyzed using two methods. In the first method we used the measured integrated line intensities to produce a population diagram (alias Boltzmann plot or rotational diagram) of each detected molecule to extract the respective total column density N_C and rotational temperature T_{rot}. The second method utilizes the eXtended CASA Line Analysis Software Suite (XCLASS)[9] by Möller et al. (2017) and in particular the myXCLASS program to model our data. Similar to the above-mentioned method myXCLASS assumes local thermodynamic equilibrium (LTE), and thus the two methods give quantities that can be directly compared with each other.

[6] APEX 12 m project E-096.C-0780A-2015.
[7] IRAM 30 m project ID: 097-15, run 003-16.
[8] GILDAS is a software provided and maintained by the Institute de Radioastronomie Millimétrique (IRAM): http://www.iram.fr/IRAMFR/GILDAS

Table 6. Observational results at H_2CO frequency positions.

Obs. (center) frequency [MHz]	rms [mK]	v_{lsr} [km s^{-1}]	*FWHM* [km s^{-1}]	$\int T_{mb} dv$ [K km s^{-1}]
R CrA-IRS 5A				
218 222.192	42.9	5.52	1.40(4)	2.821(5)
218 475.632	11.8	5.47	1.35(4)	0.266(7)
218 760.066	11.2	5.47	1.43(4)	0.325(7)
NGC 1333-IRAS 2A-1 (*center position*)				
218 222.192	23.3	(simult. fit of 3 Gaussian lines)		
		9.40(1)	3.46(24)	0.59(4)
		7.34(1)	0.53(3)	0.24(1)
		6.10^{fixed}	4.01(64)	0.24(4)
218 475.632	6.8	(simult. fit of 2 Gaussian lines)		
		7.93^{fixed}	7.3^{fixed}	0.25(1)
		7.53^{fixed}	1.0^{fixed}	0.08(1)
218 760.066	10.0	(simult. fit of 2 Gaussian lines)		
		8.0^{fixed}	8.0^{fixed}	0.31(2)
		7.5^{fixed}	1.2^{fixed}	0.11(1)
NGC 1333-IRAS 2A-2				
218 222.192	16.1	(simult. fit of 3 Gaussian lines)		
		7.79(2)	1.27(3)	−2.15(24)
		7.71(1)	1.00(2)	1.78(23)
		4.3^{fixed}	3.85(44)	0.35(3)
NGC 1333-IRAS 2A-3				
218 222.192	20.2	(simult. fit of 2 Gaussian lines)		
		7.52(1)	0.75(5)	0.34(6)
		7.43(2)	1.63(14)	−0.46(5)
L1551-IRS 5				
145 602.949	6.6	(simult. fit of 2 Gaussian lines)		
		7.0^{fixed}	1.1(1)	0.18(3)
		5.1(2)	3.4(3)	0.30(3)
150 498.334	9.1	(simult. fit of 2 Gaussian lines)		
		7.0	1.2(1)	0.22(4)
		5.2(2)	3.6(4)	0.36(5)
L1544				
145 602.949	1.1	7.14(1)	0.5^{fixed}	0.21(1)
150 498.334		7.122(2)	0.66(1)	0.193(1)

5. Observational results and analysis

This work focuses on the analysis of molecular emission from species relevant to test our shell model (see Sect. 2), namely H_2CO and CH_3OH[10], and the observational results are listed in Tables 6 and 7, respectively. Other molecular lines that we detected towards these sources within the covered band passes

[9] See https://xclass.astro.uni-koeln.de/
[10] The spectroscopic data of these molecules are based on the following works: for H_2CO see Müller & Lewen (2017) and references therein, for CH_3OH see Xu et al. (2008) and references therein.

Table 7. Observational results at CH_3OH frequency positions.

Obs. (center) frequency [MHz]	rms [mK]	v_{lsr} [km s^{-1}]	$FWHM^{(a)}$ [km s^{-1}]	$\int T_{mb}dv$ [K km s^{-1}]
R CrA -IRS 5A				
218 440.063	8.5	5.53(2)	1.33(5)	0.155(5)
318 318.919	37.3	5.34(5)	0.3^{fixed}	0.021(7)
NGC 1333-IRAS 2A-1 (center position)				
218 440.063	11.6	7.37(5)	1.9(2)	0.14(1)
[220 078.561	8.4	6.74(8)	1.9^{fixed}	0.09(5)] $^{(a)}$
318 318.919	46.2	7.2(1)	1.9(4)	0.21(3)
NGC 1333-IRAS 2A-2				
[218 440.063	13.6	7.64(2)	0.19(5)	0.012(3)] $^{(b)}$
NGC 1333-IRAS 2A-3				
[218 440.063	10.7	7.69(8)	0.5(1)	0.012(4)] $^{(b)}$
L1551-IRS 5				
145 097.435	5.0	(simult. fit of 2 Gaussian lines)		
		7.0^{fixed}	0.8^{fixed}	0.05(1)
		5.8^{fixed}	3.5^{fixed}	0.10(2)
145 103.185	4.7	(simult. fit of 2 Gaussian lines)		
		7.0^{fixed}	0.8^{fixed}	0.06(1)
		5.8^{fixed}	3.5^{fixed}	0.14(1)
L1544				
145 093.754	8.7	7.22(1)	0.51(1)	0.056(1)
145 097.435	6.7	7.18(2)	0.40(35)	0.24(1)
145 103.185	24.8	7.14(1)	0.5^{fixed}	0.41(1)

Notes. $^{(a)}$The Gaussian fit of this line resulted in $\int T_{mb}dv$ = 0.09(1) K km s^{-1}. However, from the myXClass results it seems that this line is blended with another (unknown) line, and we therefore increased the uncertainty accordingly. $^{(b)}$Unusual narrow line width for CH_3OH, should be considered with care and may be due to noise.

are not discussed further; for example, in R CrA-IRS 5A we identified lines from ^{13}CO, SO, NO, c-C_3H_2, CN isotopologues, DCN, and HCCNC.

5.1. H_2CO observations

Formaldehyde is a very common molecule in YSOs and has been observed in all four sources (see Table 6). A list of astronomically relevant formaldehyde transitions including some spectroscopic parameters is given in Table A.1. All rotational diagrams used in the following analysis of H_2CO (and also of CH_3OH) are summarized in Fig. B.4.

R CrA-IRS 5A. The observed spectra are shown in Fig. 4. Each line can be fitted well using the Gaussian line profile method. The analysis of these lines allows us to determine the temperature and column density to be around T = 27–28 K and $N_C = 4–5 \times 10^{13}$ cm^{-2}. Here, the rotational diagram method and myXCLASS results agree well. Previously, the source was investigated by Lindberg et al. (2015) with $T_{H_2CO} = 29.8 \pm 2.4$ K and $N_C = 3.7 \times 10^{13}$ cm^{-1}, which is in fair agreement with our results.

NGC 1333-IRAS 2A. This source reveals a rather complicated structure that becomes clear from its H_2CO spectra[11]. Formaldehyde has been observed at all three spatial positions (see Fig. B.1 (A) positions 1–3). For all three positions the 218.2 GHz H_2CO ($3_{0,3} - 2_{0,2}$) line can be well reproduced using three Gaussian lines fitted simultaneously. We did not analyze the line profile further, in the sense of using non-LTE, velocity gradient, or other models that take into account the internal structure of this kind of sources. Only in position 2 could the other two H_2CO lines (at 218.48 and 218.76 GHz) be observed using two Gaussian lines per observed feature. In our analysis (see Table 6) we only made use of the v_{lsr} = 7.34 km s^{-1} component. For the central position this results in $T_{rot} \approx 130 \pm 100$ K versus $T_{myXCLASS} \approx 70$ K[12] using the rotational diagram and myXCLASS, respectively,

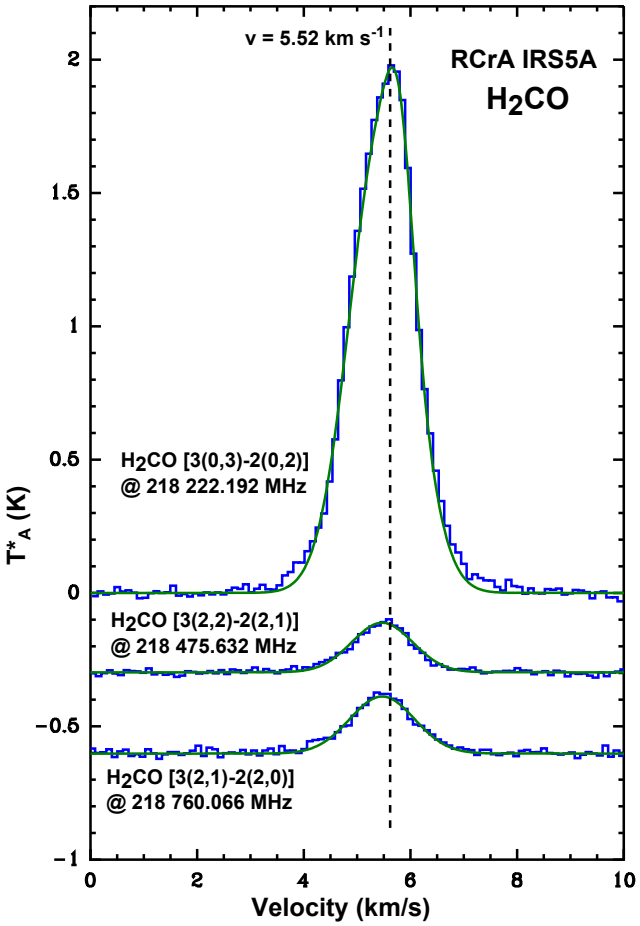

Fig. 4. H_2CO emission lines towards R CrA-IRS 5A.

[11] In position 2 (southeast) and position 3 (north) the H_2CO line is also partly seen in absorption. Absorption features of H_2CO at radio wavelengths were seen as early as 1969 (see Palmer et al. 1969) and are still in use as diagnostic tool (see Araya et al. 2014). In our case the absorption happens against the radio continuum at the mentioned source positions. As can be seen, the absorption can only be detected for the transition at 218.222 GHz which has a low-lying E_{low} = 10.5 K. For transitions with higher lying E_{low}, such as the 218.475 GHz and 218.760 GHz transitions with E_{low} = 57.6 K, no absorption can be observed.

[12] For the fit three lines are used with two lines having the same E_{up} energy (218.475 and 218.760 GHz; see Table A.1). The rotational diagram uses the average position between these two lines to fit the temperature (which results in a large uncertainty on the temperature). Contrary to this, myXCLASS fits the temperature by using the more intensive of the two lines, and thus calculates the upper limit for T and N_C.

Table 8. Comparison between observational results and model predictions.

Source	Size of emission region (model) ["]	Aver. T (model) [K]	N_c model prediction [cm^{-2}]	T_{rot} (obs) [K]	N_c (obs) [cm^{-2}]	T_{ex} (myXClass) [K]	N_c (myXClass) [cm^{-2}]
H_2CO							
R CrA-IRS 5A	64.5	18(1)	$4(3)\times10^{13}$	28.1(29)	$4.9(20)\times10^{13}$	27(7)	$4.2(6)\times10^{13}$
NGC 1333-IRAS 2A-1	66.6	19(1)	$2(1)\times10^{14}$	[132(102)	$2.57(3)\times10^{13}$]$^{(a)}$	69.0(1)	$1.64(1)\times10^{13}$
L1551-IRS 5	91.8	19(1)	$5(3)\times10^{13}$	19.0(1)	$2.1(2)\times10^{12}$	17.1(3)	$2.3(3)\times10^{12}$
L1544	114.3	12.5$^{(b)}$	$5(2)\times10^{13}$	13.1(1)	$1.8(3)\times10^{12}$	12(2)	$1.6(3)\times10^{12}$
CH_3OH							
R CrA-IRS 5A	64.5	18(1)	$3(2)\times10^{13}$	15.7(6)	$6.5(6)\times10^{13}$	18^{fixed}	$4.6(2)\times10^{13}$
NGC 1333-IRAS 2A-1	66.6	18(1)	$5(1)\times10^{14}$	69(44)	$8.8(53)\times10^{13}$	18$^{fixed,(c)}$	$3.7(1)\times10^{13}$
L1551-IRS 5	91.8	18(1)	$3(2)\times10^{13}$	3.6(7)$^{(b)}$	$1.1(10)\times10^{13}$ $^{(d)}$	6.7(1)	$6.1(1)\times10^{12}$
L1544	114.3	12.5$^{(b)}$	$2(2)\times10^{13}$	6.5(16)	$2.9(18)\times10^{13}$	6.5(3)	$2.6(2)\times10^{13}$

Notes. $^{(*)}$Recommended model values. The indicated uncertainties are due to age uncertainties of the sources, boundary conditions of the chosen integration limits (r_{start} and r_{end}), and temperature and density uncertainties of the initial parameters. $^{(**)}$Column densities are obtained by applying the rotational diagram technique. $^{(a)}$The rotational diagram made use of the $v = 7.34$ km s^{-1} component of the 218.222 GHz line and the 7.5 km s^{-1} component of the 218.475 and 218.760 GHz lines of H_2CO. $^{(b)}$Value taken from Tafalla et al. (1998). $^{(c)}$Higher temperatures lead to incorrect results in the 318 GHz spectral range. $^{(d)}$Two observed lines at 145.097 and 145.103 GHz are used for the rotational diagram analysis, as well as the three non-detected lines (integrated rms level) at 143.865, 145.093, and 146.368 GHz.

and $N_{C,rot} = 2.6\times10^{13}$ cm^{-2} and $N_{C,myXCLASS} = 1.6\times10^{13}$ cm^{-2}. Previous studies by Maret et al. (2004) came to similar results concerning the column denisty (i.e., $N_{thin} = 3\times10^{13}$ cm^{-2}) using a rotational diagram. However, their analysis used $T_{rot} = 24$ K, and with corrections for optical opacity they got $N_C = 1\times10^{14}$ cm^{-2}. Furthermore, they also analyzed the H_2CO lines using their large velocity gradient (LVG) code[13] (i.e., under non-LTE conditions) which resulted in $T_{gas} = 70$ K and $N_C = 5\times10^{13}$ cm^{-2}, which is close to our value.

L1551-IRS 5. Also for this source the line profile of H_2CO reveals a more complex structure of the source (see Fig. B.2 (A)). From the partial similarity of the line profiles of H_2CO and CH_3OH to those discussed for CO in L1551 by Snell et al. (1980) it seems like we also probed part of a molecular outflow in the southwest region of L1551-IRS 5 and associated shock regions. Thus, each of the lines at 145.6 and 150.5 GHz was fitted using two Gaussian lines. Five other transitions of H_2CO that also lie in the observed frequency region could not be detected. Our analysis resulted in $T = 19$ K and $N_C = 2\times10^{12}$ cm^{-2} for the rotational diagram method, and T=17 K and $N_C = 2\times10^{12}$ cm^{-2} using myXCLASS. Early H_2CO observations by Sandqvist & Bernes (1980) using 6 cm, 2 cm, and 2 mm H_2CO emissions from the L1551 region resulted in decreasing temperatures from 23 (center region) to 10 K (cloud periphery) and $N_{C,average} = 5\times10^{13}$ cm^{-2}. Later McCauley et al. (2011) re-analyzed H_2CO towards IRS 5 using the National Radio Astronomy Observatory (NRAO) Green Bank Telescope at 28.9 and 48.2 GHz. They used LVG analysis and assumed a temperature of $T_K \approx 100$ K resulting in $N_C \approx 3$–4×10^{13} cm^{-2}. Due to the use of different telescopes, frequencies, and slightly different source center positions a comparison between our results and these results is not straightforward.

L1544. The spectra of this source have been measured in frequency switching mode only (see Fig. B.3 (A)). Compared to the other sources the line widths are narrow (~0.6 km s^{-1}) and our analysis resulted in a temperature of T = 12–13 K, which is equal to or slightly higher than previous data with $T \approx 10$–12.5 K (e.g., Tafalla et al. 1998; Caselli et al. 2002). In Young et al. (2004)[14] the temperature is assumed to increase from 7 (core) to 13 K (periphery). Our inferred column density of $N_C = 1$–2×10^{12} cm^{-2} is very low. Young et al. (2004)[15] indicated a strong depletion effect at the inner core of the source, and previous models of L1544 by Aikawa et al. (2003)[16] also showed a strong depletion of gas-phase H_2CO on 0–4000 AU scales.

5.2. CH_3OH observations

In all our observed sources the existence of methanol could be confirmed as summarized in Table 7. The results are listed in Table 8. Relevant spectroscopic information of CH_3OH transitions can be found in Table A.1.

R CrA-IRS 5A. The CH_3OH $4_{2,2}$–$3_{1,2}$ transition at 218.4 GHz could be clearly detected (see Fig. 5) and fitted using a Gaussian line shape, whereas the non-detection of the $8_{1,7}$–$8_{0,8}$ transition at 318.3 GHz was used to infer the temperature and column density to be $T \approx 16$ K (rotational diagram) with $N_C = 5$–7×10^{13} cm^{-2} [17]. Lindberg et al. (2015) measured CH_3OH in this source having $T = 18\pm3$ K and $N_C = 3.7\times10^{13}$ cm^{-2}, which is close to our observed values.

NGC 1333-IRAS 2A. Three transitions of methanol could be detected towards position 1 (central position), see Fig. B.1 (B). At the other positions only faint signals at the $4_{2,2}$–$3_{1,2}$ transition were detected and none at the other

[13] See Ceccarelli et al. (2002) for their model implementation.

[14] See Fig. 15 in Young et al. (2004) where they used an energetics code for a model of L1544.

[15] Their source position is slightly different from ours.

[16] Assuming a 10 K temperature of the source.

[17] Using myXClass it was not possible to uniquely determine the CH_3OH temperature. Thus, in Table 8 we used the model temperature 18 K to determine N_C (myXClass).

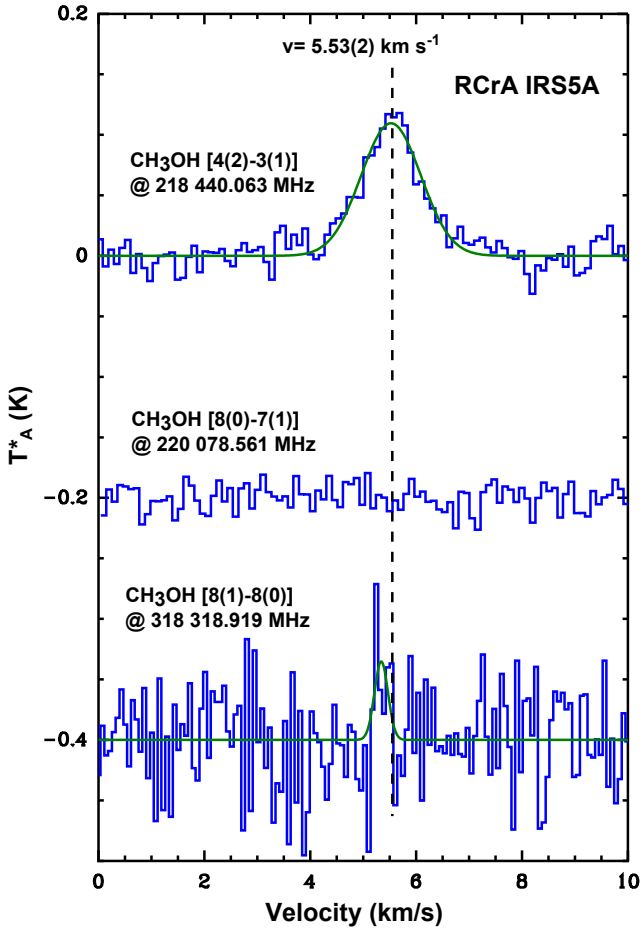

Fig. 5. CH_3OH transitions towards R CrA-IRS 5A.

frequencies, thus only the position 1 data could be used to deduce reliable T and N_C values. Unlike the H_2CO signal, it is not clear whether the methanol signal of this source originates from a simple or more complex environment. The spectra can be fitted using a simple Gaussian profile. Using our LTE rotational diagram approach, we estimate T to be around 70 ± 45 K with $N_C \approx (9 \pm 5) \times 10^{13}$ cm^{-2}. When using myXCLASS and assuming our model value temperature of 18 K[18] we get $N_C \approx 4 \times 10^{13}$ cm^{-2}. Maret et al. (2005) found CH_3OH at 101 ± 16 K in this source with $N_C = (3.4 \pm 0.6) \times 10^{14}$ cm^{-2} [19].

L1551-IRS 5. In this source two transitions of CH_3OH at 145 GHz could be observed (see Fig. B.2 (B)). Similar to the H_2CO lines discussed earlier, the CH_3OH line profile reveals internal source dynamics. Five transitions remained undetected. For the analysis only the 7 km s^{-1} component was used. The rotational diagram analysis results in $T \approx 4$ K and $N_C = 1 \times 10^{13}$ cm^{-2} [20]. The myXCLASS method results in $T \approx 7$ K and $N_C = 6 \times 10^{12}$ cm^{-2}. Previous observations by Buckle & Fuller (2000) also resulted in very low temperatures of $T \approx 3.72(76)$ K, but with a higher column density of $N_C = 7.69(78) \times 10^{13}$ cm^{-2}. White et al. (2006) modeled the L1551-IRS 5 as a circumbinary torus assuming methanol temperatures below 20 K and expected N_C between 1 and 2×10^{13} cm^{-2} for radii larger than 4000 AU starting from the IRS 5 center.

L1544. In this calm source we detected three narrow (*FWHM* of 0.4–0.5 km s^{-1}) methanol lines around 146.1 GHz in the frequency switching mode (see Fig. B.3 (B)). No lines could be seen at the two other CH_3OH frequency positions (i.e., at 143.9 and 146.4 GHz). The rotational diagram analysis and the myXCLASS analysis result in $T \approx 7$ K and $N_C \approx 3 \times 10^{13}$ cm^{-2}. Bizzocchi et al. (2014) observed methanol at $T_{ex} = 6 \pm 3$ K with $N_C = (1.9 \pm 1.9) \times 10^{13}$ cm^{-2} using an LTE approach and also made a non-LTE analysis resulting in $N_C = (2.7 \pm 0.6) \times 10^{13}$ cm^{-2}. Vastel et al. (2014) reported values of $T_k = 10$ K with $N_t = 3 \times 10^{13}$ cm^{-2} using non-LTE LVG analysis. Thus, the previous methanol values derived by other groups and our values are in good agreement.

In summary, the H_2CO and CH_3OH data resulting from the new observations presented here and those available from the literature are found to be in good agreement. With the new observations, a set of well-defined data was obtained, which was used for our comparative studies. However, for sources such as NGC 1333-IRAS 2A and L1551-IRS 5, where earlier data did not yield consistent temperature values for the molecules investigated here, no significant improvement could be achieved, as originally hoped for.

6. Discussion

The results of the observations are summarized and compared to the predicted values by our physical chemical shell model in Table 8.

R CrA-IRS 5A (Class 1). This source proved to be well suited for our applied shell model. The spectra are not dominated by internal source dynamics (e.g., outflows) and allow a straightforward analysis. The observed and predicted column densities of H_2CO and CH_3OH agree within a few 10^{13} cm^{-2}. The measured temperatures of CH_3OH agree within 2–3 K with the predicted ≈18 K. However, the H_2CO temperature shows a deviation of $T_{obs}(27\text{–}28\ \text{K}) - T_{model}(18\ \text{K}) \approx 10$ K of yet unknown reason. In a simple gradient model, H_2CO is much warmer than our model predicts, which corresponds to a formaldehyde distribution much closer to the protostar than expected (around 1000 AU). However, we cannot simply assume a higher H_2CO temperature in our model without further consequences for other species such as CH_3OH. An as-yet-unknown H_2CO specific heating mechanism may be at play, but this is beyond our model assumptions, and thus remains incomprehensible. As can be seen when comparing the modeled values in Tables 4 and 8 for H_2CO, the gradient model column density value is better by about a factor two with respect to the flat model value, whereas the temperatures are nearly identical for both models and show the same deviation with respect to the observed temperature. However, for CH_3OH the flat model tends to be closer to the observed column density.

NGC 1333-IRAS 2A (Class 0). Because of the inner structure and dynamics, the deviation between the modeled shell structure and the observed geometry is stronger than in any other of the sources investigated here. To compare the observations with the model, certain assumptions (like the restriction to the $v_{lsr} = 7.34$ km s^{-1} component of the multi-peak molecular transition lines) had to be made. The observed column densities of H_2CO and CH_3OH (≈10^{13} cm^{-2}) are not in agreement with the predicted value (≈10^{14} cm^{-2}). Even so, it should be noted that the

[18] For this source myXCLASS has problems fitting T and N_C simultaneously. Thus T_{model} is used.
[19] They also found that their measured temperature is very high, and discussed this in their work; see Maret et al. (2005) Sect. 4.1.
[20] By using the undetected lines to restrict the solution space.

gradient model column density value is closer to observations than the flat model value. On first sight, our observed high temperatures for formaldehyde (> 69 K) or methanol (≈69 K), which are partly in agreement with previous works, show that there may be a discrepancy between our assumed temperature profile based on SED observations, which basically reflects the dust conditions in this source and the gas-phase species investigated here. However, the temperature assignment remains difficult, as can be seen from the work of Maret et al. (2004) where temperatures vary between 24 and 70 K for H_2CO depending on the analysis method (e.g., using non-LTE analysis methods). In addition, our model does not indicate why the dust and gas-phase temperature should be decoupled. For this source the predictions of the gradient and flat model do not deviate much for H_2CO and are equally off with respect to the observed temperature and column density. However, for the CH_3OH column density the gradient model is slightly closer to the observations.

L1551-IRS 5 (Class 1). In this source we have a mixed situation when comparing the observations and the model results. In our analysis we restricted ourselves to the narrow v_{lsr} = 7.0 km s^{-1} component of the lines[21]. H_2CO shows a depletion with observed column densities as low as a few 10^{12} cm^{-2} compared to the predicted $N_T = 5 \times 10^{13}$ cm^{-2}. The derived rotational temperatures of formaldehyde (≈17–19 K) are close to the predicted 19 K of the model. Similar to NGC 1333-IRAS 2A the spectra reveal dynamical and most likely non-LTE processes within this source. The column density of methanol is predicted by the model with an order of magnitude difference, which is not very accurate, as is the temperature ($\Delta T_{obs-model} \approx 11$–14 K). The observed very low temperatures of CH_3OH of 3.6–6.7 K contrast with the assumed mean temperature of 18 K from the model. For both, H_2CO and CH_3OH, the column densities of the gradient model are closer to observations than the flat model values.

L1544 (pre-stellar core). Previous work by Tafalla et al. (1998) suggests that this source contains molecules at low temperatures. Constrained by their data we used our model to predict the H_2CO and CH_3OH abundances. The H_2CO observations confirmed the low temperature, but the model predicted an order of magnitude higher column density for H_2CO in the gas-phase than observed. At the same time the observed column density of CH_3OH fits nicely to the model values, although the temperature is off by a factor of two and close to the assumed inner core temperature by Young et al. (2004) and the 6 K value reported by Bizzocchi et al. (2014). It is not clear why the observations show a depletion of H_2CO (at least for the observed transitions) and not for CH_3OH. When trying to model different physical parameters, for example density and temperature gradient within reasonable values, it is not possible to explain the discrepancies between the observed and the model abundance. Even when assuming other source ages than 5×10^4 yr within a range of 1×10^4 yr to 1×10^5 yr the observed abundances of H_2CO and CH_3OH cannot be modeled consistently.

7. Conclusions

A new physical model has been developed and tested that assumes a simple spherical geometry with a density and temperature gradient and combines this with a chemical model (Du et al. 2012) including gas-grain interactions. As test species we used the ice-borne molecules H_2CO and CH_3OH, but also provided model data for HOOH and H_2O, which are discussed elsewhere (Fuchs et al. 2020). Four astronomical sources were chosen in which formaldehyde, methanol, and also water have already been detected.

Our model is most reliable when the source is not dominated by jets or shock regions (which we intentionally did not include in the model) and when the source is not too young. It works well for the quiescent Class 1 object R CrA-IRS 5A. For the young pre-stellar core L1544 no jets and shocks are at play, and our predictions are nearly independent of its geometry. However, the H_2CO depletion and the discrepancy between the modeled and observed temperatures of CH_3OH show that our chemical model is imprecise when applied to this source (opposed to the L1544 model from Aikawa et al. 2003 which is specifically designed for collapsing pre-stellar cores). For sources (Class 0 and Class 1) with contributions of outflows or shock regions (e.g., NGC 1333-IRAS 2A-1 and L1551-IRS 5) the model is not well suited.

From a theoretical point of view, the applied shell model is an improvement compared to the previously used flat model when modeling objects with spherical gradient distributions of density and temperature, like YSOs of Class 0-1. Our model yields smaller column densities and abundances for H_2CO and CH_3OH in comparison to a flat model with a constant H_2 density and temperature. The geometry effect does not usually change the expected column densities dramatically, i.e., by orders of magnitude, but rather by factors between 2 and 8. This still means that a better signal-to-noise ratio (S/N) is needed, i.e., longer integration times have to be considered. Our new gradient model results are generally closer to the observational results when compared to those predicted by the flat model.

Acknowledgements. We thank the APEX 12 m and IRAM 30 m staff for their excellent support. We thank Peter Schilke, Thomas Möller and Álvaro Sánchez-Monge for their kind introduction to myXCLASS.

[21] We include these values for the sake of completeness. The broad v_{lsr} = 5.1 km s^{-1} second components result in T_{H_2CO} = 18.4 K and $N_{H_2CO} = 3.1 \times 10^{12}$ cm^{-2} and T_{CH_3OH} = 25.5 K and $N_{CH_3OH} = 1.9 \times 10^{13}$ cm^{-2}.

References

Aikawa, Y., Ohashi, N., & Herbst, E. 2003, ApJ, 593, 906
Ainsworth, R. E., Coughlan, C. P., Green, D. A., et al. 2016, MNRAS, 462, 2904
Allen, M., & Robinson, G. W. 1977, ApJ, 212, 396
Araya, E. D., Dieter-Conklin, N., Goss, W. M., & Andreev, A. 2014, ApJ, 784, 129
Bergman, P., Parise, B., Liseau, R., et al. 2011, A&A, 531, L8
Bizzocchi, L., Caselli, P., Spezzano, S., & Leonardo, E. 2014, A&A, 569, A27
Boogert, A. C. A., Pontoppidan, K. M., Knez, C., et al. 2008, ApJ, 678, 985
Boogert, A. C. A., Gerakines, P. A., & Whittet, D. C. B. 2015, ARA&A, 53, 541
Bottinelli, S., Ceccarelli, C., Williams, J. P., & Lefloch, B. 2007, A&A, 463, 601
Bottinelli, S., Boogert, A. C. A., Bouwman, J., et al. 2010, ApJ, 718, 1100
Brinch, C., Jorgensen, J. K., & Hogerheijde, M.R. 2009, A&A, 502, 199
Bruderer, S., Doty, S. D., & Benz, A. O. 2009a, ApJS, 183, 179
Bruderer, S., Benz, A. O., Doty, S. D., et al. 2009b, ApJ, 700, 872
Buckle, J. V., & Fuller, G. A. 2000, ESA SP 445, 339
Caselli, P., Hasegawa, T. I., & Herbst, E. 1993, ApJ, 408, 548
Caselli, P., Walmsley, C. M., Zucconi, A., et al. 2002, ApJ 565, 344
Caselli, P., Keto, E., Bergin, E. A., et al. 2012, ApJ, 759, L37
Caux, E., Kahane, C., Castets, A., et al. 2011, A&A, 532, A23
Cazaux, S., Minissale, M., Dulieu, F., & Hocuk, S. 2016, A&A, 585, A55
Ceccarelli, C., Baluteau, J.-P., Walmsley, M., et al. 2002, A&A, 383, 603
Chuang, K.-J., Fedoseev, G., Ioppolo, S., et al. 2016, MNRAS, 455, 1702
Chuang, K.-J., Fedoseev, G., Qasim, D., et al. 2018, ApJ, 853, 102
Close, L.M., Roddier, F., Northcott, M. J., et al. 1997, ApJ, 478, 766
Crapsi, A., Caselli, P., Walmsley, C. M., et al. 2005, ApJ, 619, 379
Crapsi, A., Caselli, P., Walmsley, M. C., & Tafalla, M. 2007, A&A, 470, 221
Cuppen, H. M., Ioppolo, S., & Linnartz, H. 2010, Phys. Chem. Chem. Phys., 12, 12077
Doty, S.D., van Dishoeck, E. F., van derTak, F. F. S., & Boonman, A. M. S. 2002, A&A, 389, 446
Du, F., & Parise, B. 2011, A&A, 530, A131

Du, F., Parise, B., & Bergman, P. 2012, A&A, 538, A91
Duncan, R. A., Forster, J. R., Gardner, F. F., & Whiteoak, J. B. 1987, MNRAS, 224, 721
Fedoseev, G., Chuang, K.-J., Ioppolo, S., et al. 2017, ApJ, 842, 52
Fuchs, G. W., Cuppen, H. M., Ioppolo, S., et al. 2009, A&A, 505, 629
Fuchs, G. W., Witsch, D., Herberth, D., et al. 2020, A&A, 636, A114
Garrod, R. T. 2008, A&A, 491, 239
Garrod, R. T., Widicus Weaver, S. L., & Herbst, E. 2008, ApJ, 682, 283
Hasegawa, T. I., & Herbst, E. 1993, MNRAS, 261, 83
Hasegawa, T., Herbst, E., & Leung, C. M. 1992, ApJS, 82, 167
Hiraoka, K., Sato, T., Sato, S., et al. 2002, ApJ, 577, 265
Hogerheijde, M. R., & Sandell, G. 2000, ApJ, 534, 880-893
Ioppolo, S., van Boheemen, Y., Cuppen, H. M., et al. 2011, MNRAS, 413, 2281
Ivezic, Z., & Elitzur, M. 1997, MNRAS, 287, 799
Jiménez-Serra, I., Vasyunin, A. I., Caselli, P., et al. 2016, ApJ, 830, L6
Jørgensen, J. K., Hogerheijde, M. R., van Dishoeck, E. F., et al. 2004, A&A, 413, 993
Jørgensen, J.K., Bourke, T.L., Myers, P.C., et al. 2005, ApJ, 632, 973
Kristensen, L. E., van Dishoeck, E. F., Bergin, E. A., et al. 2012, A&A, 542, A8
Lee, J.-E., Lee, J., Lee, S., et al. 2014, ApJS, 214, 21
Lee, J.-E., Lee, S., Baek, G., et al. 2019, Nat. Astron., 3, 314
Leung, C. M., Herbst, E., & Huebner, W. F. 1984, ApJS, 56, 231
Lindberg, J. E., & Jørgensen, J. K. 2012, A&A, 548, A24
Lindberg, J. E., Jørgensen, J. K., Watanabe, Y., et al. 2015, A&A, 584, A28
Lucas, P. W., & Roche, P. F. 1997, MNRAS, 286, 895
Maret, S., Ceccarelli, C., Caux, E., et al. 2004, A&A, 416, 577
Maret, S., Ceccarelli, C., Tielens, A. G. G. M., et al. 2005, A&A, 442, 527
McCauley, P. I., Mangum, J. G., & Wootten, A. 2011, ApJ, 742, 58
Minissale, M., Dulieu, F., Cazaux, S., & Hocuk, S. 2016, A&A, 585, A24
Millar, T. J., Macdonald, G. H., & Gibb, A. G. 1997, A&A, 325, 1163
Möller, T., Endres, C., & Schilke, P. 2017, A&A, 598, A7
Mottram, J. C., Kristensen, L. E., van Dishoeck, E. F., et al. 2014, A&A, 572, A21
Müller, H. S. P., & Lewen, F. 2017, J. Mol. Spectr., 331, 28
Osorio, M., D'Alessio, P., Muzerolle, J., et al. 2003, ApJ, 586, 1148
Padgett, D. L., Brandner, W., Stapelfeldt, K. R., et al. 1999, ApJ, 117, 1490
Palmer, P., Zuckerman, B., Buhl, D., & Snyder, L. E., et al. 1969, ApJ, 156, L147
Pickett, H. M., Poynter, R. L., Cohen, E. A., Delitsky, M. L., et al. 1998, J. Quant. Spectr. Rad. Transf, 60, 883
Punanova, A., Caselli, P., Feng, S., et al. 2018, ApJ, 855, 112
Robitaille, T. P., Whitney, B. A., Indebetouw, R., & Wood, K. 2007, ApJS, 169, 328
Sandell, G., Knee, L. B. G., Aspin, et al. 1994, A&A, 285, L1
Sandqvist, Aa., & Bernes, C. 1980, A&A, 89, 187
Schmalzl, M., Visser, R., Walsh, C., et al. 2014, A&A, 572, A81
Smith, R. G., Charnley, S. B., Pendleton, Y. J., et al. 2011, ApJ, 743, 131
Snell, R. L., Loren, R. B., & Plambeck, R. L. 1980, ApJ, 239, L17
Schöier, F. L., Jørgensen, J. K., van Dishoeck, E. F., & Blake, G. A. 2002, A&A, 390, 1001
Stantcheva, T., & Herbst, E. 2004, A&A, 423, 241
Stäuber, P., Doty, S. D., van Dishoeck, E. F., & Benz, A. O. 2005, A&A, 440, 949
Tafalla, M., Mardones, D., Myers, P. C., et al. 1998, ApJ, 504, 900
Taylor, K. N. R., & Storey, J. W. V. 1984, MNRAS, 209, 5
Tielens, A. G. G. M., & Hagen, W. 1982, A&A, 114, 245
Vastel, C., Ceccarelli, C., Lefloch, B., & Bachiller, R. 2014, ApJ, 795, L2
Watanabe, N., & Kouchi, A. 2002, AJ, 571, L173
White, Glenn J., Fridlund, C. W. M., Bergman, P., et al. 2006, ApJ, 651, L41
Whittet, D. C. B., Schutte, W. A., Tielens, A. G. G. M., et al. 1996, A&A, 315, L357
Woodall, J., Agúndez, M., Markwick-Kemper, A., & Millar, T. 2007, A&A, 466, 1197
Xu, L.-H., & Lovas, F. J. 1997, J. Phys. Chem. Ref. Data, 26, 17
Xu, L.-H., Fisher, J., Lees, R. M., et al. 2008, J. Mol. Spectr., 251, 305
Young, K. E., Lee, J.-E., Evans II, N. J., et al. 2004, ApJ, 614, 252

Appendix A: Additional tables

Table A.1. Selection of relevant transitions of H_2CO, and CH_3OH for cold environments in the (80–320 GHz) submm region.

Transition	Frequency	log (intensity) at 300 K	A_{ul}	E_{up}	Upper state degeneracy
$(J_{K_a,K_c} - J'_{K'_a,K'_c})$	[MHz]	[nm^2 MHz]	[s^{-1}]	[K]	$g_{up} = g_I \cdot g_k$
H_2CO (g_I=1: para; g_I=3: ortho)					
$[13_{2,11} - 13_{2,12}$	*89 565.0597	−9.2706	9.299×10^{-7}	368.668	$27 = 1 \cdot 27]$ [(a)]
$2_{1,2} - 1_{1,1}$	140 839.5020	−2.9775	5.301×10^{-5}	21.9	$15 = 3 \cdot 5$
$2_{0,2} - 1_{0,1}$	*145 602.9490	−3.2841	7.809×10^{-5}	10.5	$5 = 1 \cdot 5$
$2_{1,1} - 1_{1,0}$	*150 498.3340	−2.9206	6.468×10^{-5}	22.6	$15 = 3 \cdot 5$
$3_{1,3} - 2_{1,2}$	211 211.4680	−2.3879	2.270×10^{-4}	32.1	$21 = 3 \cdot 7$
$3_{0,3} - 2_{0,2}$	*218 222.1920	−2.7693	2.816×10^{-4}	21.0	$7 = 1 \cdot 7$
$[3_{2,2} - 2_{2,1}$	*218 475.6320	−3.0917	1.570×10^{-4}	68.1	$7 = 1 \cdot 7]$ [(a)]
$[3_{2,1} - 2_{2,0}$	*218 760.0660	−3.0906	1.576×10^{-4}	68.1	$7 = 1 \cdot 7]$ [(a)]
$3_{1,2} - 2_{1,1}$	*225 697.7750	−2.3318	2.770×10^{-4}	33.5	$21 = 3 \cdot 7$
$4_{1,4} - 3_{1,3}$	281 526.9290	−2.0074	5.879×10^{-4}	45.6	$27 = 3 \cdot 9$
$4_{0,4} - 3_{0,3}$	290 623.4050	−2.4132	6.897×10^{-4}	34.9	$9 = 1 \cdot 9$
$4_{1,3} - 3_{1,2}$	300 836.6350	−1.9524	7.175×10^{-4}	47.9	$27 = 3 \cdot 9$
CH_3OH ((ν_t Parity) $J_{K_a,K_c} - J'_{K'_a,K'_c}$ ((ν_t' Parity') A & $E_{1/2}$ symmetry) [(b)]					
(0+) $2_{0,2} - 1_{0,1}$ (0+) A	96 741.371	−4.9799	3.408×10^{-6}	7.0	$5 = 1 \cdot 5$
(0) $2_{0,2} - 1_{0,1}$ (0) E_1	96 744.545	−4.9990	3.407×10^{-6}	20.1	$5 = 1 \cdot 5$
(0+) $3_{1,3} - 2_{1,2}$ (0+) A	*143 865.795	−4.5391	1.069×10^{-5}	28.3	$7 = 1 \cdot 7$
(0) $3_{0,3} - 2_{0,2}$ (0) E_1	*145 093.754	−4.4793	1.231×10^{-5}	27.1	$7 = 1 \cdot 7$
(0) $3_{-1,3} - 2_{-1,2}$ (0) E_2	*145 097.435	−4.5191	1.096×10^{-5}	19.5	$7 = 1 \cdot 7$
(0+) $3_{0,3} - 2_{0,2}$ (0+) A	*145 103.185	−4.4600	1.232×10^{-5}	13.9	$7 = 1 \cdot 7$
(0−) $3_{1,2} - 2_{1,1}$ (0−) A	*146 368.328	−4.5244	1.125×10^{-5}	28.6	$7 = 1 \cdot 7$
[(0) $4_{2,2} - 3_{1,2}$ (0) E_1	*218 440.063	−3.9915	4.686×10^{-5}	45.5	$9 = 1 \cdot 9]$ [(a)]
[(0) $8_{0,8} - 7_{1,6}$ (0) E_1	*220 078.561	−4.0627	2.516×10^{-5}	96.6	$17 = 1 \cdot 17]$ [(a)]
[(0−) $8_{1,7} - 8_{0,8}$ (0+) A	*318 318.919	−3.3698	1.793×10^{-4}	98.8	$17 = 1 \cdot 17]$ [(a)]

Notes. All values are taken from the JPL catalog (Pickett et al. 1998) (entry: 30004 H_2CO; 32003 CH_3OH). Frequencies marked with an asterisk [(*)]are transitions that have been observationally investigated. g_I is the spin-statistical weight and g_k is the upper state spin-rotational degeneracy (2J+1). [(a)]Although these are weaker lines, they are relevant because they are part of this observation. [(b)]See Xu et at. (1997).

Appendix B: Additional figures

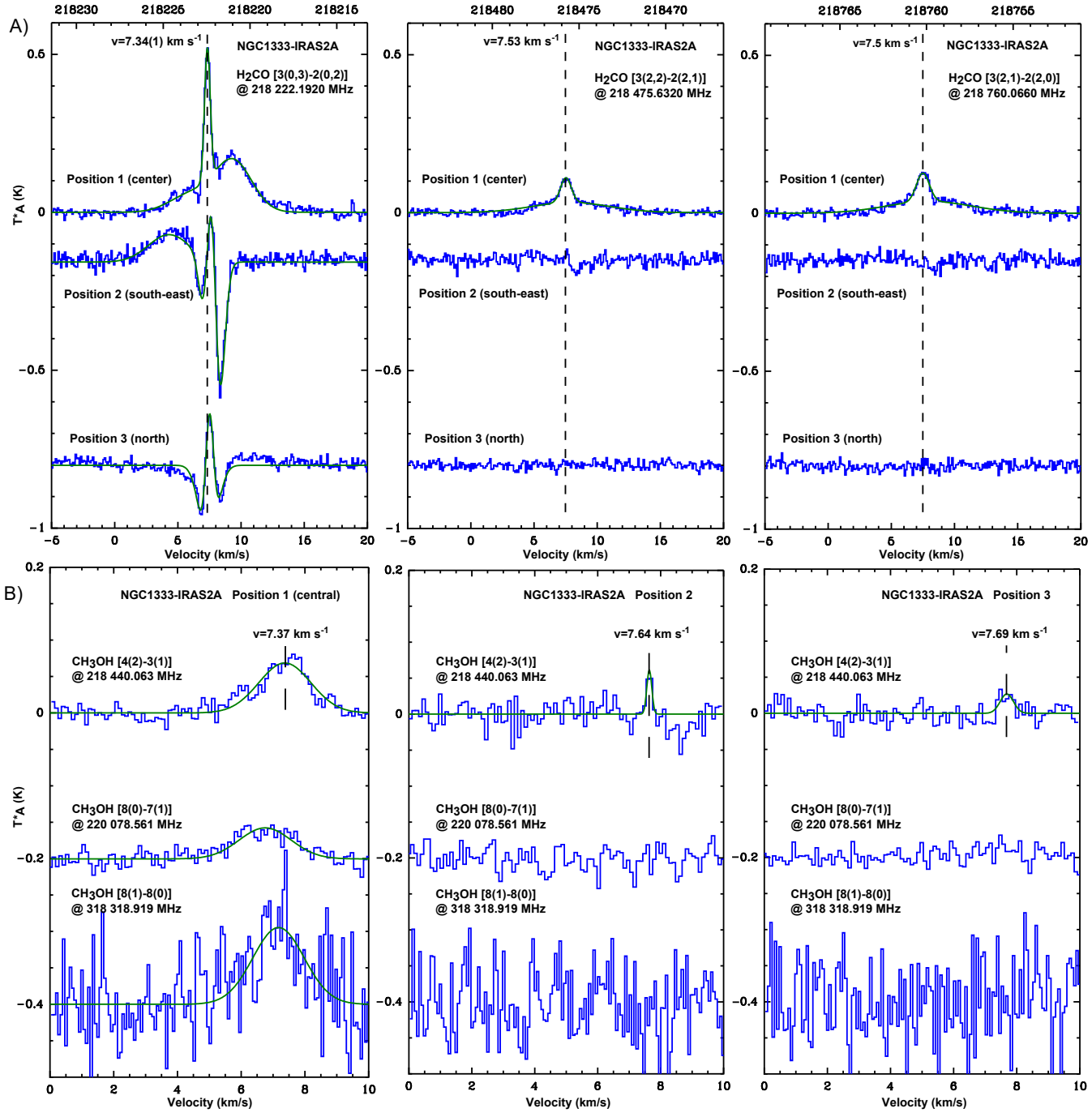

Fig. B.1. Molecuar transitions towards NGC 1333-IRAS 2A position 1–3. (*A*) H_2CO and (*B*) CH_3OH.

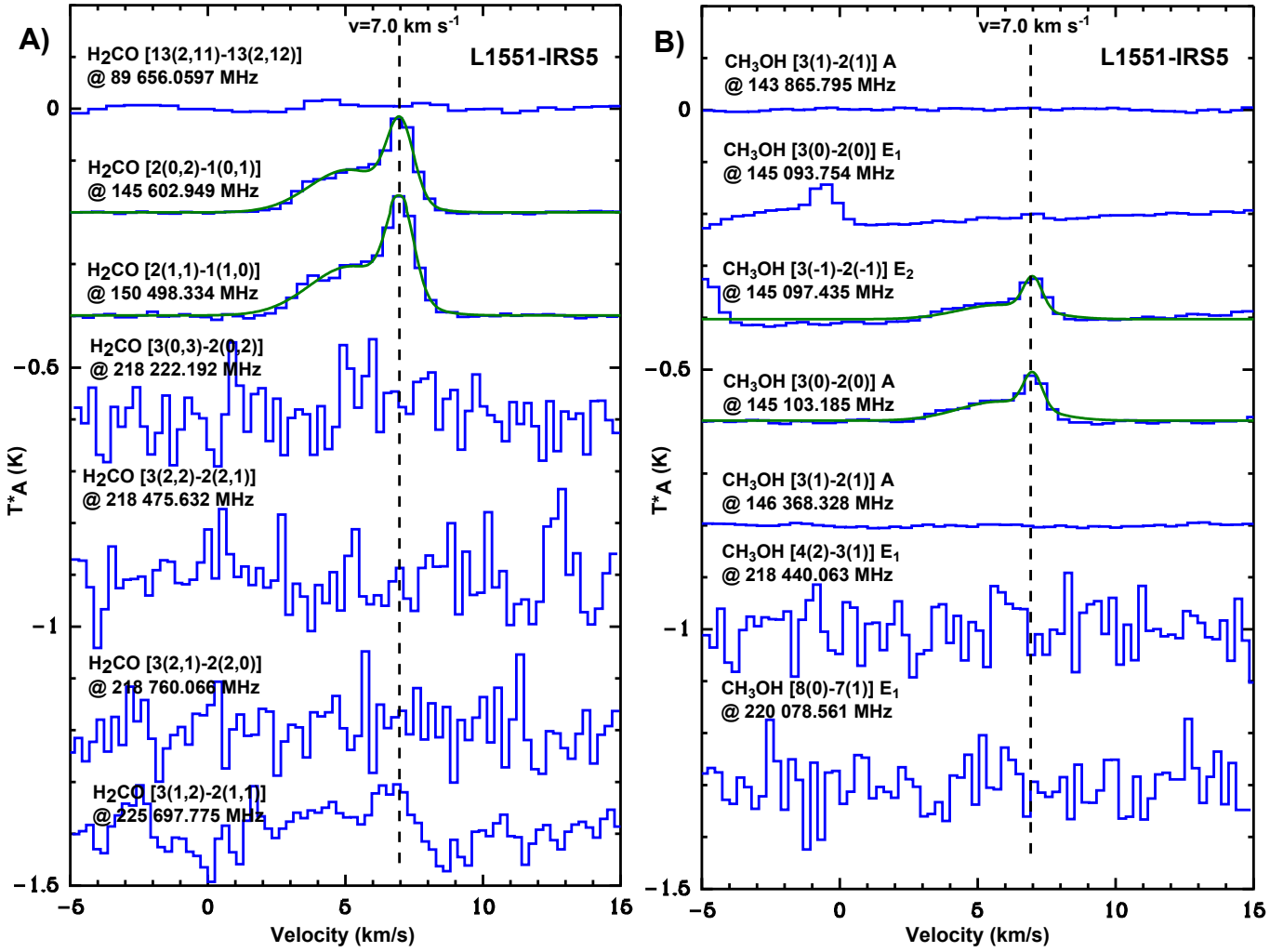

Fig. B.2. Observations towards L1551-IRS 5 using position switching mode. (*A*) and (*B*) show H_2CO and CH_3OH transitions taken in position switching mode, respectively.

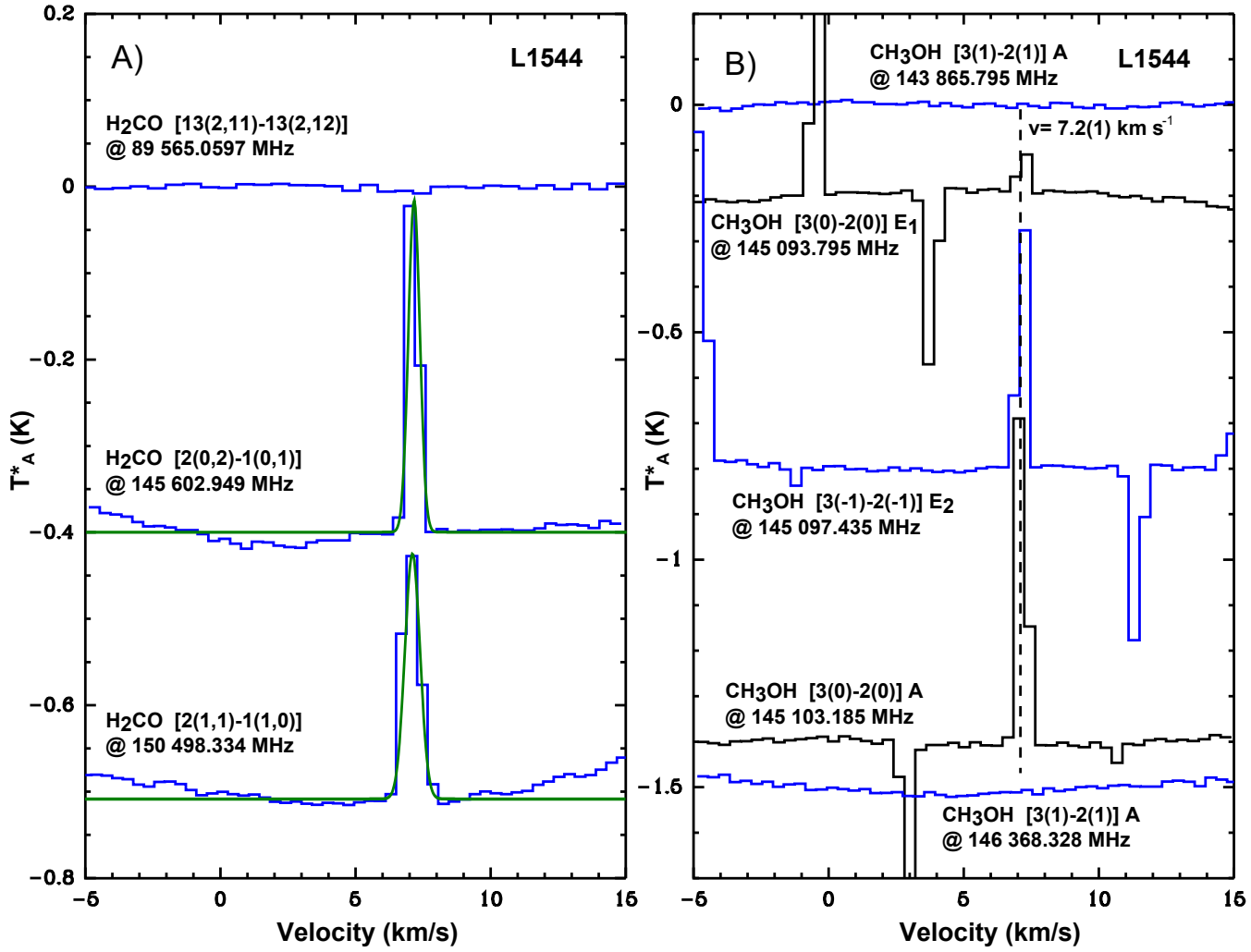

Fig. B.3. Molecular transitions towards L1544 (frequency switching mode): (*A*) H_2CO and (*B*) CH_3OH.

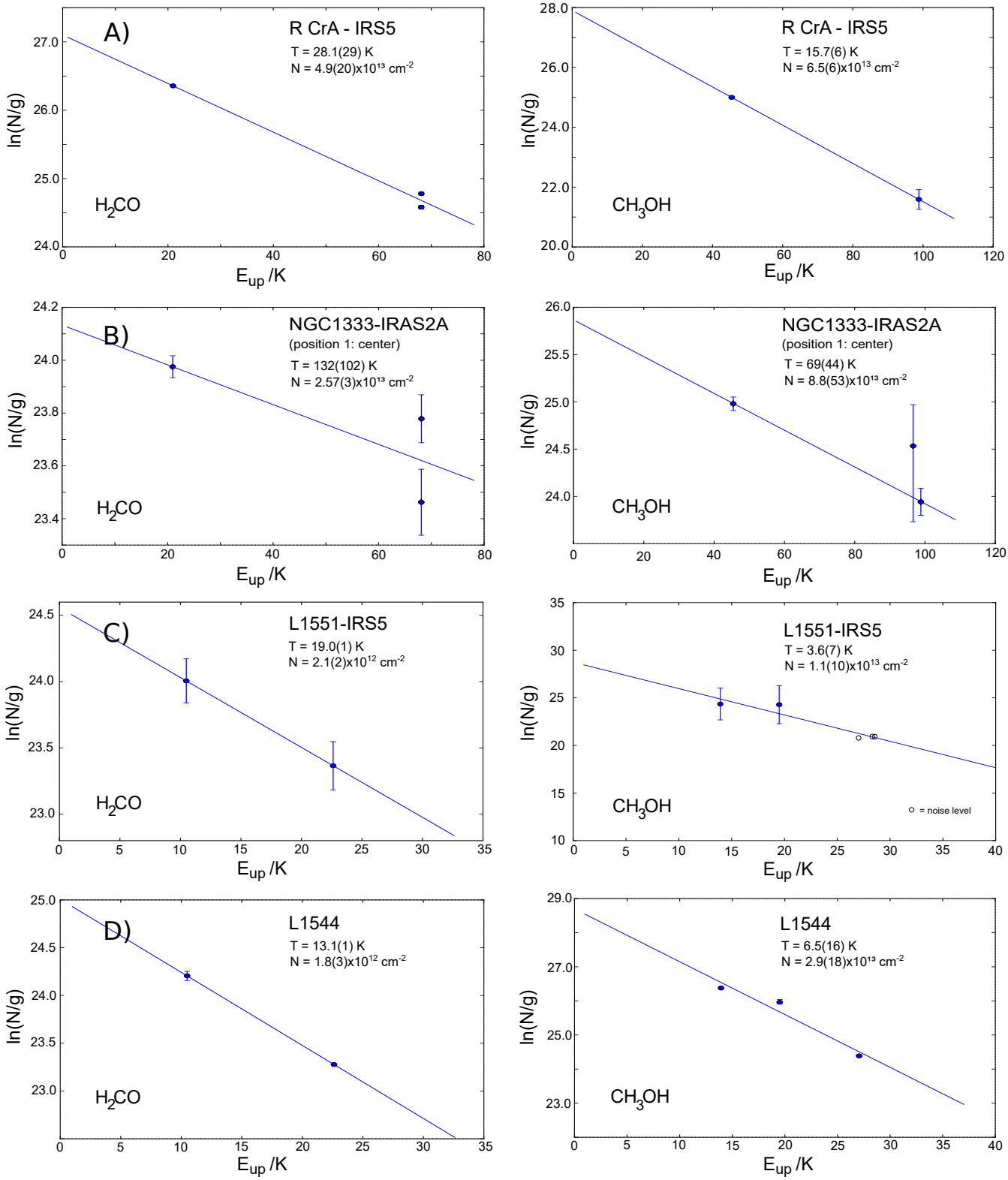

Fig. B.4. Rotational diagrams of H_2CO (*left*) and CH_3OH (*right*) emission from (*A*) R CrA-IRS 5A, (*B*) NGC 1333-IRAS 2A, (*C*) L1551-IRS 5, and (*D*) L1544.